Journal of Translational Medicine

RESEARCH

Open Access

Integrative multi-omics analysis reveals the role of tumor-associated endothelial cells and their signature in prognosis of intrahepatic cholangiocarcinoma

Hao Jiang[1,2,3†], Biao Gao[1,2,3,4†], Zihe Meng[3,5†], Yafei Wang[6], Tianyu Jiao[1,2,3], Junfeng Li[1,2,3], Xuerui Li[1,2,3,4], Yinbiao Cao[1,2,3], Xianzhou Zhang[7*], Chonghui Li[1,2,3*] and Shichun Lu[1,2,3*]

Abstract

This study aims to investigate the interplay between tumor-associated endothelial cells (TECs) and immune cells within the tumor microenvironment (TME) and its impact on tumor prognosis. We conducted single-cell RNA sequencing (scRNA-seq) of tumor, normal, and lymph node tissues obtained from intrahepatic cholangiocarcinoma (ICC) patients to reveal the role of TECs in tumor angiogenesis and their significant heterogeneity. Meanwhile, we identified genes highly expressed in TECs and constructed TEC signatures (TEC.Sig). Next, we calculated TEC scores of samples based on TEC.Sig. Patients with higher TEC scores exhibited a higher frequency of KRAS mutations, which was associated with increased infiltration of neutrophils and immature dendritic cells (iDCs), and decreased numbers of natural killer (NK), CD4 + T, and CD8 + T effector memory (Tem) cells, indicating an inflammation-dominated immunosuppressive phenotype. In contrast, BAP1 mutations and CXCL12 overexpression showed a contrasting trend. Spatial transcriptomics analysis and histological experiments further confirmed that TECs interacted with various tumor-killing immune cells through the CXCL12/CXCR4 axis. Multiple tumor immunotherapy datasets confirmed that the TEC.Sig could predict patient responses to immunotherapy. The TEC score is a promising and reliable biomarker for predicting genetic mutations and prognosis in ICC patients. Enhancing the regulation of the CXCL12/CXCR4 signaling pathway may represent a potential novel therapeutic target for ICC treatment.

Keywords Intrahepatic cholangiocarcinoma (ICC), Tumor microenvironment (TME), Tumor-associated endothelial cell (TEC), Single-cell RNA sequencing (scRNA-seq), CXCL12, Biomarker

†Hao Jiang, Biao Gao and Zihe Meng have contributed equally to this work.

*Correspondence:
Xianzhou Zhang
zzu12345@163.com
Chonghui Li
lichonghui@301hospital.com.cn
Shichun Lu
lushichun@301hospital.com.cn
[1] Medical School of Chinese People's Liberation Army (PLA), Beijing, China
[2] Faculty of Hepato-Pancreato-Biliary Surgery, The First Medical Center of Chinese PLA General Hospital, Beijing, China
[3] Key Laboratory of Digital Hepatobiliary Surgery of Chinese PLA, Beijing, China
[4] Nankai University School of Medicine, Nankai University, Tianjin, China
[5] College of Basic Medical Science, Inner Mongolia Medical University, Hohhot, Inner Mongolia Autonomous Region, China
[6] Department of Hepatobiliary Surgery, The First Affiliated Hospital of Henan University of Science and Technology, Luoyang, China
[7] Department of Hepatic Biliary Pancreatic Surgery, Cancer Hospital Affiliated to Zhengzhou University, Zhengzhou 450000, Henan, China

Introduction

Intrahepatic cholangiocarcinoma (ICC) is the second most common malignant liver tumor after hepatocellular carcinoma (HCC) [1, 2]. Currently, radical surgical resection (R0 resection) remains the only potential curative treatment for ICC [3]. However, due to the occult onset of ICC, most patients miss the optimal timing for R0 resection at diagnosis. Even after undergoing radical hepatectomy, the five-year survival rate of ICC patients is only approximately 30%, with a high recurrence rate of 60–70% [4, 5]. Therefore, an in-depth exploration of prognostic factors that facilitate patient risk stratification and clinical decision-making is particularly important.

The TME encompasses both the internal and external environments crucial for tumor development and progression, influencing aspects such as immune evasion and treatment resistance [6]. Histologically, ICC is characterized by a dense fibro-inflammatory stroma composed of fibroblasts, infiltrating immune cells, endothelial cells, and extracellular matrix components supporting tumor progression [7, 8]. TECs are pivotal cells within the tumor stroma that can promote tumor cell immune escape, proliferation, and metastasis [9]. TECs participate in TME matrix formation and angiogenesis, while also regulating interactions between tumor cells and immune cells through the secretion of cytokines, chemokines, and growth factors [10, 11]. In recent years, the development of novel anti-cancer strategies, such as immunotherapy and anti-angiogenic drugs, which show promising effects against multiple tumor types, has mainly focused on the targeting of the tumor stroma [12–15]. However, the response and survival benefits associated with these treatment modalities are limited to only a few patients due to the heterogeneity and complexity of the TME [16]. Therefore, a deep understanding of the interactions within the ICC immune microenvironment and the identification of potential therapeutic targets are crucial for predicting immunotherapy responses, evaluating efficacy, discovering prognostic markers, and guiding individualized treatment strategies.

Here, we performed the scRNA-seq analysis of tumor and lymph node tissues obtained from an ICC patient following surgical resection. We then integrated our data with a published ICC scRNA-seq dataset (GSE89749), including five tumor samples, three normal samples, and one lymph node sample. We successfully identified TECs and uncovered their significant functional heterogeneity. Interestingly, we found that TECs can activate immune cells through the CXCL12/CXCR4 axis, demonstrating anti-tumor properties. Meanwhile, we extracted a gene set specific to TECs and constructed the TEC score at the bulk RNA level, for predicting ICC patient prognosis and stratification. Immunocyte infiltration analysis showed that ICC patients with high TEC scores had more infiltrating neutrophils and iDCs in the TME. Thus, they presented with an inflammation-dominant immunosuppressive phenotype. Further research found that hepatitis B infections and BAP1 mutations were associated with an immune-activated phenotype in the TME, thereby promoting anti-tumor immune responses. Finally, we found that the TEC.Sig could effectively predict the response of cancer patients to immunotherapy, helping identify non-responders. Overall, our findings could help stratify ICC patients based on long-term survival prospects and identify individuals who benefit from immunotherapy, thereby avoiding unnecessary adverse drug reactions in patients not benefiting from immunotherapy.

Materials and methods

Data and clinical samples

An ICC patient diagnosed histologically was enrolled in this study. The patient underwent tumor and lymph node resection at the First Medical Center of the People's Liberation Army General Hospital, and scRNA-seq of the resected specimens was performed. Informed consent was obtained from the patient, allowing the collection of samples for research and genomic analysis. To increase sample size, we downloaded scRNA-seq data (GSE138709) from five ICC patients, including three adjacent normal tissues and four tumor tissues, and integrated it with our data using the Harmony algorithm. Additionally, gene expression data and complete clinical information were obtained from 244 ICC patients participating in the study by Dong et al. [17]. In the validation set, we collected clinical data from 155 ICC patients who underwent surgical resection at the Henan Cancer Hospital Department of Hepatobiliary and Pancreatic Surgery from February 2013 to October 2019, and were pathologically diagnosed after surgery. Furthermore, transcriptomic data and related clinicopathological data of 83 ICC patients were obtained from the Gene Expression Omnibus (GEO) database (accession number: GSE89749). Additionally, we collected high-resolution spatial transcriptomic data from the study by Rui Wu et al. [http://lifeome.net/supp/livercancer-st/data.htm].

Tissue isolation and cell purification

Fresh tissue samples were cut into approximately 1 cubic millimeter pieces on ice and transferred to 1.5 mL tubes containing Dulbecco's Modified Eagle Medium. Subsequently, the tissue samples were minced further and rinsed with 1×PBS. Minced tumor tissues were immediately transferred to a 15 mL tube and dissociated using a tissue dissociation kit. The suspension was filtered through a 70-micron cell strainer and centrifuged at 400 g for 5 min, after which the supernatant was

removed. Next, the sample was treated with red blood cell lysis buffer for 5 min, filtered through a 40-micron cell strainer, and washed twice with 1 × PBS. Finally, the viability of cells in the tissue samples was assessed using trypan blue staining. Single cells, reagents, and gel beads containing cell barcodes were encapsulated into nanoliter gel bead emulsions using the BMKMANU-DG1000 platform. The cDNA library was constructed using the Chromium Single Cell 3′ Library & Gel Bead Kit v3. Qualitative analysis was conducted using high-sensitivity DNA assays on the Agilent Bioanalyzer. The final library was sequenced on the Illumina NovaSeq 6000 sequencing system.

Analysis pipeline

Cell Ranger v3.1 was used to align and quantify scRNA-seq data with the human reference genome GRCh38, generating a gene expression matrix. Raw output data were processed using the R package Seurat (v4.1.2), which filtered out cells with fewer than 200 detected genes or more than 10% mitochondrial gene content. The R package "Harmony" was used to integrate single-cell data, using default parameters for cell clustering analysis. The Seurat object was processed with SCTransform, and dimensionality reduction was performed using Principal Component Analysis (PCA). The first 30 principal components were used for subsequent cell clustering analysis. Major cell clusters were determined using the FindNeighbors and FindClusters functions. t-Distributed Stochastic Neighbor Embedding (t-SNE) was used to reduce dimensionality and visualize clustering results. Finally, we collected signature genes for T cells, NK cells, epithelial cells, myeloid cells, B cells, fibroblasts, circulating cells, and endothelial cells from the Azimuth database (https://azimuth.hubmapconsortium.org/references/). Using these genes, we precisely annotated the cell clusters by analyzing their differential expression across the clusters.

Identification of endothelial cell subpopulations

To identify endothelial cell subpopulations, we extracted UMI counts from 1634 endothelial cells. To mitigate batch effects and reduce patient-specific biases, we applied the Harmony algorithm. For dimensionality reduction and subtype identification, we selected the top 2000 highly variable genes using the FindVariableFeatures function and normalized the data. We then performed PCA based on these variable genes. Using the FindNeighbors function, we constructed a nearest-neighbor graph based on the top 30 principal components, followed by clustering with the FindClusters function (resolution = 0.1). The clusters were visualized using t-SNE, and the FindAllMarkers function was employed to identify marker genes specific to each cluster.

Identification of TEC.Sig and construction of TEC scores

The FindAllMarkers function from the Seurat package was utilized to screen for genes overexpressed in TECs. By applying the criteria of avg_log2FC > 1 and p_val_adj < 0.05, genes highly expressed in TECs were identified and defined as TEC.Sig. Subsequently, Cox univariate regression analysis was conducted to screen genes impacting the prognosis of ICC patients. LASSO regression analysis, using the R package "glmnet," was employed to pinpoint the genes most closely associated with overall survival (OS) in ICC samples. Ultimately, Cox multivariate analysis was performed to identify independent risk genes for ICC patient prognosis ($P < 0.05$) and to construct a prognostic model. The formula for constructing the TEC-related gene risk score is as follows: TEC scores = (gene 1 expression × corresponding coefficient) + … + (gene n expression × corresponding coefficient). The rfsrc function from the R package randomForestSRC was utilized to rank the importance of variables. The 244 ICC patients were then stratified into high TEC score and low TEC score groups based on the median TEC scores. Finally, survival differences between the two groups were compared using the R packages "survival" and "survminer".

Functional and gene enrichment analyses

To explore the functional and pathway enrichment associated with TEC scores, we performed Gene Set Enrichment Analysis (GSEA) using the GSEA software. Based on the "c2.cp.kegg.v7.4.symbols" gene set from the MSigDB database and HALLMARK gene set, differences in pathways and molecular mechanisms were assessed between the high and low TEC score groups. Subsequently, the R package "clusterProfiler" was used for gene ontology (GO) analysis of differentially expressed genes, with a p-value threshold of 0.05.

Immunocyte infiltration analysis

To evaluate the differences in the immune and stromal cell infiltration between the high and low TEC score groups, we used xCell (https://comphealth.ucsf.edu/app/xcell) to calculate the proportion of these cells in each ICC sample.

Somatic mutation analysis

We used the read.maf function from the maftools package in R to read mutation information for 244 ICC patients in MAF format. The top 20 mutated genes were acquired and presented in a waterfall plot using

the maftools package (v2.12.0) in R, which is usually applied to visualize and summarize mutated genes.

Prediction of response to immunotherapy

Tumor Immune Dysfunction and Exclusion (TIDE) analysis was used to explore the response to immunotherapy during cancer treatment. TIDE (http://tide.dfci.harvard.edu/) was also used to predict the immunotherapy response based on two major tumor immune escape mechanisms: T cell dysfunction and reduced T cell infiltration. We collected mRNA expression data and corresponding clinical information from 17 HCC patients receiving anti-PD1 treatment (N = 17, responders vs non-responders = 8 vs 9) from the GEO database (https://www.ncbi.nlm.nih.gov/geo/query/acc.cgi?acc=GSE202069). Additionally, we collected data from 103 melanoma patients receiving immunotherapy (N = 103, responders vs non-responders = 46 vs 57), from a study conducted by Liu et al. [5]. Similarly, data for 298 bladder cancer patients receiving immunotherapy (N = 298, responders vs non-responders = 68 vs 230) were obtained from the IMvigor210 dataset [18]. To validate the ability of TEC.Sig to predict the immunotherapy response, we calculated the Z-scores of tumor patients receiving immunotherapy using the R package cancerclass. Subsequently, we assessed the predictive performance of these Z-scores on immunotherapy outcomes by employing receiver operating characteristic (ROC) curves.

Ligand–receptor expression and cell interactions

Cell–cell communication was determined by assessing the expression of ligand–receptor pairs in cell populations. We used the R package CellChat to study interactions between different cell types, with a gene expression threshold of 0.2 as the cutoff.

Multicolor immunofluorescence

Formalin-fixed, paraffin-embedded tissue Sects. (4 μm thick) were mounted on glass slides and baked at 65 °C for 2 h. Sections were deparaffinized in xylene and rehydrated through graded ethanol. Antigen retrieval was performed in citrate buffer (pH 6.0) using microwave treatment. Endogenous peroxidase activity was quenched with 3% hydrogen peroxide for 15 min at room temperature, and non-specific binding was blocked with goat serum for 30 min.

Sections were incubated overnight at 4 °C with primary antibodies (100 μL each): SOF1 (1:1000, 17402-1-AP), CD79 (1:1000, AF20163), CD8 (1:1000, AF20211), and VWF (1:2000, ET1701-87). The next day, sections were incubated with HRP-conjugated secondary antibodies for 30 min at room temperature.

Subsequently, sections were labeled with TSA fluorescent dyes (TYR-570, TYR-520, TYR-620, TYR-690) in separate reactions, each for 3–10 min, followed by washing with PBST. These steps were repeated for each antibody. Nuclei were counterstained with DAPI for 10 min, washed with PBS, and mounted with anti-fade medium. Slides were imaged using a multi-channel fluorescence scanner. ImageJ was used to quantify the relative fluorescence intensity of each marker, followed by correlation analysis between CXCL12 and CD8A + T cells and CD79A + B cells using GraphPad Prism.

Spatial transcriptomics analysis

The gene-spot matrices generated from ST and Visium samples were processed using the Seurat package (v4.1.2) in R. Spots with fewer than 200 detected genes were filtered out, and genes with fewer than 10 read counts or expression in fewer than three spots were excluded. Normalization across spots was performed using the LogNormalize function. Dimensionality reduction and clustering were conducted using principal component analysis based on the first 30 principal components. To enhance the visualization of spatial expression patterns, the spots were refined using the "spatialEnhance" function from the BayesSpace package (v1.6.0), and expression features were further enhanced with the "enhanceFeatures" function. Additionally, signature scores derived from the scRNA-seq dataset were incorporated into the metadata of the ST dataset using the "AddModuleScore" function with default settings in Seurat.

Statistical analysis

All statistical analyses were performed using R software (v4.1.2) and GraphPad Prism 9. Differences in survival between the two groups were assessed using Kaplan–Meier curves and log-rank tests. Univariate and multivariate Cox regression analyses were used to identify factors affecting prognosis. Pearson's correlation coefficient was used for normally distributed data in correlation analysis, while Spearman's correlation coefficient was used for non-normally distributed data. Differences between two groups were compared using the unpaired Student's t-test or Wilcoxon rank-sum test. The R package "pROC" was used to plot ROC curves to verify the validity of the TEC score and determine the area under the curve (AUC). The Benjamini–Hochberg method was utilized to adjust p-values, with $P < 0.05$ indicating statistical significance.

Results

Landscape of the TME in ICC

To elucidate the cellular composition of the TME and abdominal lymph nodes in ICC, we obtained tumor and

abdominal lymph node samples from a patient. Fresh tissues were rapidly processed into single-cell suspensions and subjected to scRNA-seq. Given the limited sample size, we integrated our data with previously published scRNA-seq datasets on ICC to gain deeper insights into the TME. This analysis ultimately included five tumor samples, three normal samples, and one lymph node sample. To eliminate batch effects between samples, we used the Harmony package in R to integrate data from different samples. To remove low-quality cells and doublets (droplets containing two cells), we filtered out cells with fewer than 200 unique molecular identifiers (UMIs) or those with fewer than 200 or more than 8000 expressed genes per cell. We also excluded cells with over 10% mitochondrial gene UMI content to eliminate dead or dying cells. This process yielded scRNA-seq data for 79,797 high-quality cells (Figures S1A–C). Unsupervised clustering identified multiple cell clusters (Fig. 1A) without significant batch effects across samples (Fig. 1B). These clusters were classified into T cells, NK cells,

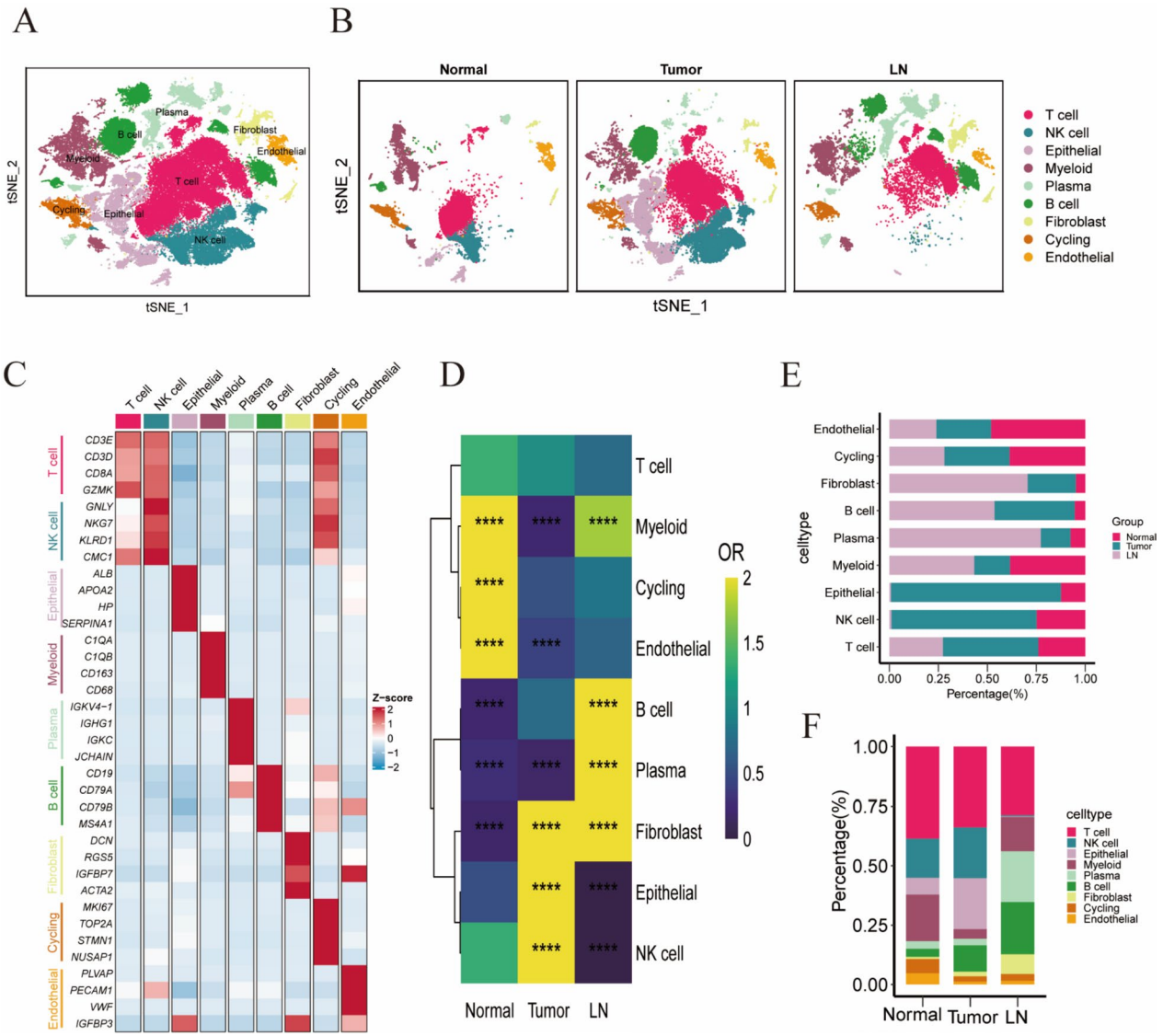

Fig. 1 Immunological infiltration landscape within the TME of ICC. **A** t-SNE dimensionality reduction plot depicting the distribution of distinct cell populations after integrating tumor, normal, and lymph node samples from ICC patients. **B** t-SNE plot illustrating the distribution of cell populations within normal tissue, tumor tissue, and lymph node samples. **C** Heatmap showing the expression of canonical marker genes specific to each cell type. **D** Odds ratio (OR) heatmap comparing the abundance of each cell type across normal tissue, tumor tissue, and lymph node samples. **E** Proportional distribution of cell types in normal tissue, tumor tissue, and lymph node samples. **F** Bar graphs illustrating the proportions of each cell type within normal tissue, tumor tissue, and lymph node samples

epithelial cells, myeloid cells, B cells, fibroblasts, circulating cells, and endothelial cells based on canonical marker gene expression (Fig. 1C, S1D). Notably, the distribution of these eight cell types varied significantly across samples: NK and epithelial cells were predominantly found in tumor tissues, while B and plasma cells were mainly in lymph nodes (Figs. 1D–F). We observed a significant increase in NK cells and fibroblasts in ICC tumor tissues compared to normal tissues, potentially linked to cytokine recruitment within the TME. Endothelial cells were more enriched in normal tissues than in tumor tissues, but their numbers are limited in both. Given the lack of research on ICC endothelial cells, we explored their potential role in the TME.

Heterogeneity of TECs in the TME of ICC

In ICC tumor tissues, there is abundant blood supply, characterized by a high number of blood vessels with complex structures, affecting the metabolic and immunological status of the TME [19–21]. These tissues exhibit elevated levels of pro-angiogenic factors that activate TECs, thereby playing a pivotal role in the TME [22–24]. Therefore, we analyzed the role of TECs in the TME.

A total of 1643 TECs with significant heterogeneity were identified. Through clustering analysis, all TECs were categorized into five distinct cell clusters: MGP+Endo, NPIPB4+Endo, FCGR2B+Endo, IGLC3+Endo, and PDPN+Endo (Fig. 2A). ROGUE was used to precisely quantify the purity of the identified endothelial cell subpopulations, ensuring a robust and sensitive assessment of their homogeneity (Figure S1E). The distribution of endothelial cell subpopulations showed significant variation across tissues (Fig. 2B). MGP+Endo and FCGR2B+Endo were predominantly enriched in normal tissues, while NPIPB4+Endo and IGLC3+Endo were primarily enriched in lymphatic tissues. PDPN+Endo and a subset of NPIPB4+Endo were mainly found in tumor tissues.

Pathway enrichment analysis revealed that genes overexpressed in these cells were primarily associated with angiogenesis and extracellular matrix remodeling (Fig. 2C). Each endothelial cell cluster exhibited a distinct gene expression pattern (Fig. 2D–E): The MGP+Endo cluster is characterized by the upregulation of genes involved in immune cell interactions (SELE, SELP, VCAM1), collagen production (COL4A1, COL4A2), and angiogenesis (INSR, SPARC), and is enriched in the "positive regulation of cell adhesion" pathway. The FCGR2B+Endo cluster shows increased expression of genes associated with the inflammatory response (IL1B, IL1R1, CCL3, CCL4), indicating its role in inflammation. The NPIPB4+Endo and IGLC3+Endo clusters overexpress genes linked to lymphocyte activation (CXCR4, IKZF3, PTPRC, TNFAIP3) and collagen (COL4A1, COL4A2), with enrichment in pathways regulating and activating immune responses, suggesting these lymph node-derived endothelial cells play a significant role in immune regulation. The PDPN+Endo cluster, predominantly found in tumor tissue, upregulates genes involved in extracellular matrix interactions (ITGB1, LGALS1) and angiogenesis (ANGPT2, FLT4), highlighting its involvement in these processes.

Establishment and validation of a three-gene prognostic signature based on TEC marker genes

Characteristic gene expression-related alterations in TECs within the TME precisely regulate their proliferation, migration, and vascular structural stability [25–29]. The aberrant expression of these genes can promote abnormal angiogenesis and potentially lead to tumor progression and poor prognosis [30, 31]. To investigate the impact of TEC-specific genes on prognosis, we selected 206 genes that were highly expressed in TECs based on the following criteria: avg_log2FC > 1 and P_val_adj < 0.05. Through Cox univariate regression analysis, we further identified 79 genes that significantly influenced ICC patient prognosis ($P < 0.05$, Supplementary Table 1). Subsequently, we employed LASSO regression analysis to determine the key variables most associated with OS. To enhance the accuracy of the model, we set the number of iterations for the algorithm to 1000. In addition, we utilized the cv.glmnet function for tenfold cross-validation,

(See figure on next page.)

Fig. 2 Characterization and functional analysis of endothelial cell populations. **A** t-SNE dimensionality reduction plot depicting the distribution of endothelial cells after integrating tumor, normal, and lymph node samples from ICC patients. **B** OR heatmap comparing the abundance of endothelial cells across normal tissue, tumor tissue, and lymph node samples. **C** Enrichment analysis of highly expressed genes in endothelial cells. **D** Expression patterns of functionally relevant genes across different endothelial cell subpopulations, demonstrating their characteristics in various functional pathways. **E** GO functional enrichment analysis results of characteristic genes in endothelial cell subpopulations, presented as dot plots. **F**–**G** Distribution plots of the partial likelihood deviation and coefficient of LASSO regression. **H** Forest plot from Cox multivariate regression analysis, identifying three independent prognostic-related genes by analyzing the relationship between each gene and the HR with a CI of 95%. **I** Heatmap illustrating the correlation between TEC scores and survival time. **J** Bar graph showing the importance ranking of gene variables in the random forest model. **K** Kaplan–Meier survival curves comparing high and low TEC score groups, indicating a poorer prognosis for the high TEC score group

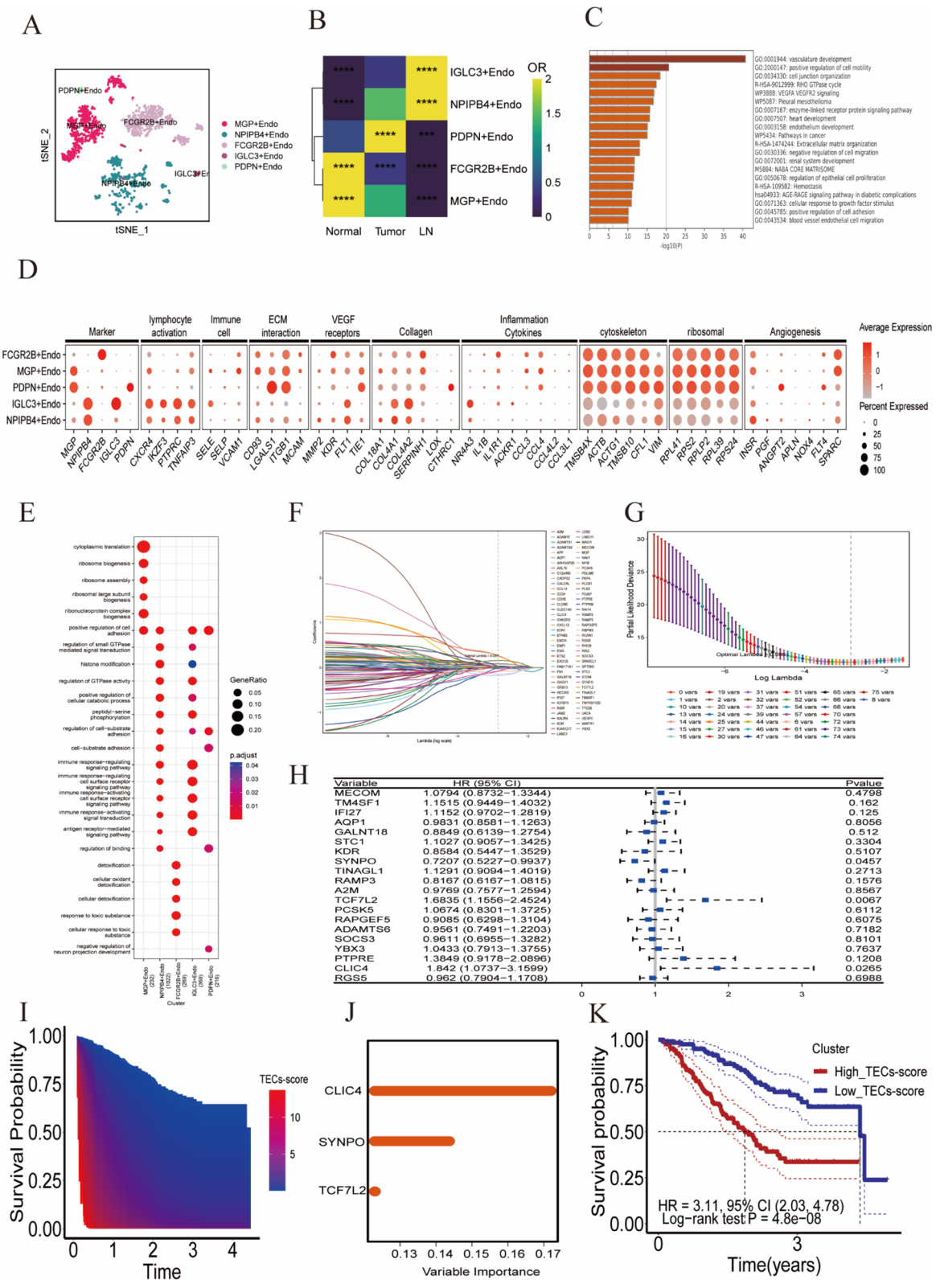

Fig. 2 (See legend on previous page.)

to reduce the risk of model overfitting. Ultimately, at a lambda.min value of 0.0351, we selected 19 variables with non-zero coefficients (Figs. 2F–G). Through Cox multivariate regression analysis of these 19 variables, three genes were identified as independent prognostic factors for ICC patients ($P < 0.05$, Fig. 2H).

The genes TCF7L2, CLIC4, and SYNPO are highly expressed in endothelial cells and show a certain level of specificity (Figure S1F-G). The TEC score indicated the expression levels of these three genes, and was calculated as follows: 0.6872 × TCF7L2 expression + 0.9846 × CLIC4 expression − 0.5397 × SYNPO expression.

We discovered that the prognosis of ICC patients worsened with an increase in the TEC scores (Figs. 2I and S2A). The results of random forest survival analysis indicated that the CLIC4 expression level was the most significant variable contributing to the TEC score (Fig. 2J). Using the median TEC score value, we classified 244 ICC patients into high and low TEC score groups. Kaplan–Meier curve analysis confirmed the poorer prognosis in the high TEC score group compared to the low TEC score group (hazard ratio [HR] = 3.11, 95% confidence interval [CI]: 2.03–4.78, P = 4.8e-08, Fig. 2K). Time-dependent ROC analysis showed AUC values of 0.754 and 0.785 for predicting OS at 1 and 3 years, respectively, and was used to assess the predictive ability of TEC scores (Figure S2B). In the GSE89749 validation set, ICC patients in the high TEC score group also exhibited a poorer prognosis (Figure S2C), confirming the robustness of the TEC score for predicting ICC patient prognosis. Time-dependent ROC curves further validated the predictive efficacy of the TEC score for long-term survival in ICC patients (Figure S2D).

TEC scores and Intrahepatic metastasis were identified as reliable factors for predicting ICC patient prognosis

To thoroughly examine the association between the TEC score and the clinical features of ICC patients, we performed a comprehensive correlation analysis. The results indicated that the TEC score was not associated with patient age, sex, tumor diameter, history of gallstones, or hepatitis B surface antigen (HBsAg) status (Fig. 3A). However, it was significantly correlated with vascular invasion, perineural invasion, distant metastasis, intrahepatic metastasis, and TNM staging (Fig. 3B). Furthermore, the TEC score was significantly and positively correlated with tumor markers, including elevated levels of carbohydrate antigen 19–9 (CA19-9) and carcinoembryonic antigen (CEA) (Figure S2E–F). These findings suggest that the TEC score may be related to tumor invasiveness.

Univariate Cox regression analysis indicated that several factors significantly impacted ICC patient prognosis. These factors included intrahepatic metastasis; tumor size; microvascular invasion; regional lymph node metastasis; distant metastasis; perineural invasion; CA19-9, CEA, alanine aminotransferase (ALT), and gamma-glutamyltransferase (γ-GT) levels; TNM staging; and TEC scores (all with $P < 0.05$, Fig. 3C). Cox multivariate regression analysis further confirmed that intrahepatic metastasis, regional lymph node metastasis, ALT levels, and TEC scores were independent risk factors affecting ICC patient prognosis ($HR > 1$, $P < 0.05$, Fig. 3D).

Notably, there may be a correlation between the TEC score and the occurrence of intrahepatic metastasis, with ICC patients positive for intrahepatic metastasis showing a poorer prognosis (HR = 2.43, 95% CI 1.63–3.61, P = 5.9e-06, Fig. 3E). This suggests that both TEC scores and intrahepatic metastasis are important prognostic indicators for predicting ICC patient outcomes. To further validate this finding, we obtained clinical data from 155 ICC patients. Survival analysis revealed that patients with ICC and intrahepatic metastasis had a poorer prognosis (HR = 2.03, 95% CI 1.36–3.02, P = 0.00038, Fig. 3F). Moreover, within this dataset, intrahepatic metastasis emerged as an independent risk factor influencing the prognosis of ICC patients (Figure S2G–H), which is consistent with previous analytical results.

Finally, we constructed a nomogram for predicting the prognosis of ICC patients based on intrahepatic

(See figure on next page.)

Fig. 3 Analysis of the relationship between TEC scores, clinical characteristics, and prognosis. **A** Comparison of TEC scores among various clinical characteristics, presented as a bar graph showing the impact of factors such as age, sex, tumor diameter, history of bile duct stones, and HBsAg status on TEC scores. **B** Bar graph showing the correlation between TEC scores and tumor invasion characteristics, including vascular invasion, perineural invasion, distant metastasis, intrahepatic metastasis, and TNM staging. **C** Forest plot showing hazard ratios (HR) and p-values for various clinical characteristics, derived from Cox univariate regression analysis identifying significant factors affecting ICC patient prognosis. **D** Cox multivariate regression analysis identifying independent risk factors affecting long-term survival in ICC patients. **E** Kaplan–Meier curves illustrating the relationship between intrahepatic metastasis and survival time, comparing patients with and without intrahepatic metastasis. **F** Kaplan-Meier survival curve analysis for validation cohort 1, stratified by intrahepatic metastasis. **G** A nomogram for predicting ICC patient prognosis, incorporating factors such as intrahepatic metastasis, regional lymph node metastasis, ALT levels, and TEC scores. **H** A calibration curve to verify the predictive performance of the nomogram. **I** ROC curve assessing the predictive performance of the nomogram, with AUCs of 0.743 and 0.746 for 1-year and 3-year survival rates, respectively

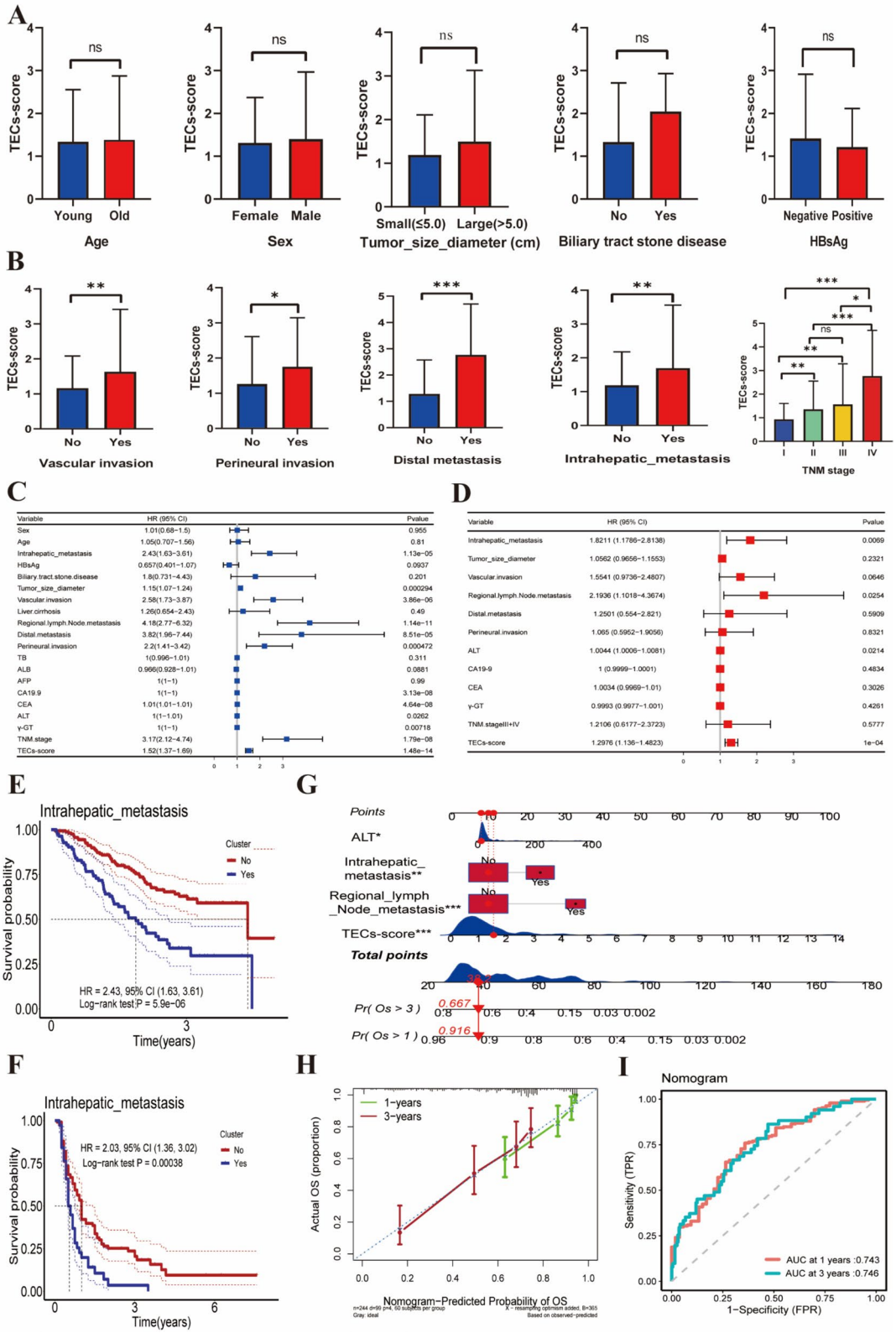

Fig. 3 (See legend on previous page.)

metastasis, regional lymph node metastasis, ALT levels, and TEC scores (Fig. 3G). Both the ROC curve and calibration curve confirmed the favorable performance of the nomogram for predicting 1-year and 3-year survival rates in ICC patients (Fig. 3H–I).

TEC scores reflect the degree of infiltration of immunosuppressive cells in the TME

To explore the mechanisms underlying the predictive capability of the TEC score, we examined its relationship with immune cell infiltration. Gene expression data from 244 ICC patients were analyzed using the xCell platform (https://comphealth.ucsf.edu/app/xcell) to assess immune cell infiltration proportions. The study revealed significant differences in immune cell infiltration between the high and low TEC score groups. The TME in the high TEC score group was predominantly infiltrated by CD8 + Tcm, DCs, MSCs, monocytes, neutrophils, Th2 cells, and iDCs, whereas the low TEC score group was mainly infiltrated by CD8 + Tem, mast cells, plasma cells, and Th1 cells (Fig. 4A). High levels of infiltration of neutrophils and Th2 cells reflected a robust inflammatory response state, suggesting that ICC patients in the high TEC score group may exhibit higher levels of inflammation.

The mRNA and protein levels of S100A family members (including S100A8/S100A11) were upregulated in the high TEC score group (Fig. 4B), potentially associated with oncogenic inflammation. GSEA enrichment analysis revealed that the high TEC score group was primarily enriched in inflammatory response, IL-6/JAK/STAT3 signaling, TGF-β signaling, and TNF-α/NF-κB signaling pathways, indicating that these tumors might be driven by underlying chronic overt or smoldering inflammation (Figure S3A–D) [32–35]. Additionally, the numbers of immunosuppressive neutrophils and iDCs were significantly increased in the TME of the high TEC score group (Fig. 4A), suggesting that ICC patients in this group may have a potent immunosuppressive microenvironment. Concurrently, increased mRNA levels of CD8A, GZMA, and PRF1 in the low TEC score group confirmed the upregulation of anti-tumor immune responses (Fig. 4C).

Kaplan–Meier curve results showed that ICC patients exhibiting high infiltration of neutrophils, Th2 cells, and iDCs had a poorer prognosis, whereas those with high infiltration of CD8 + Tem exhibited a contrasting outcome (Fig. 4D). In the ICC TME, high infiltration of neutrophils and iDCs leads to an upregulation of immunosuppressive genes (Figure S3E-F), further confirming that ICC patients in the high TEC score group may exhibit an inflammation-dominated immunosuppressive phenotype. ICC patients in the high TEC score group showed a high overlap with the immune-suppressed subgroup (IG1) reported by Lin et al. (Fig. 4E) [36].

HBV infection is a known risk factor for ICC, but the immunogenomic characteristics of HBV-associated ICC are poorly understood. Immune infiltration analysis revealed a significant increase in adaptive immune cells, including B cells, CD4 + T cells, CD4 + memory T cells, CD8 + Tem, and NK cells in the TME of HBV-positive ICC patients, with no significant difference in immunosuppressive myeloid cells (Fig. 4F). This finding indicates that HBV infection does not amplify the oncogenic inflammatory response in ICC; instead, it enhances the infiltration of cytotoxic immune cells.

Overexpression of CXCL12 and KRAS mutations affect TME neutrophil and iDC infiltration

Studies have demonstrated that the chemokine CXCL12 regulates directional leukocyte migration through its interaction with receptors CXCR4 or CXCR7 [37]. Intriguingly, we observed significantly higher CXCL12 expression levels in the low TEC score group (Figs. 5A, S3G), contrasting with the excessive infiltration of neutrophils and iDCs in the high TEC score group (Fig. 4A). As expected, patients with higher CXCL12 mRNA levels exhibited a more favorable prognosis (HR = 0.55, 95% CI 0.37–0.82, P = 0.003) (Fig. 5B). The levels of CXCL12 mRNA were negatively correlated with oncogenic factors, including VEGF, IL1A, IL1B, CXCL3, and IL-6, and positively correlated with tumor suppressive factors, including CD8A, GZMA, TBX21, and CCL5 (Fig. 5C). The CXCL12 mRNA levels were negatively associated with the infiltration of neutrophils and iDCs, and positively correlated with

(See figure on next page.)

Fig. 4 Analysis of the relationship between TEC scores and TME immune cell infiltration. **A** Bar graph comparing immune cell infiltration between high and low TEC score groups, showing differences in the proportions of various immune cells. **B** Heatmap analysis of high and low TEC score groups, illustrating the mRNA and protein expression levels of S100A family members in both groups. **C** Heatmap showing differences in markers that promote or inhibit cancer inflammation at the mRNA level between high and low TEC score groups. **D** Kaplan–Meier curves illustrating the relationship between immune cell composition in the TME and survival time, highlighting the impact of different immune cell infiltrates on patient survival. **E** Sankey diagram of TME cell composition between different risk groups, demonstrating the difference in immune cell composition between the high and low TEC score groups. **F** Bar graph comparing TME cell compositions based on HBV infection status, illustrating differences in immune cell proportions between HBV-positive and negative patients

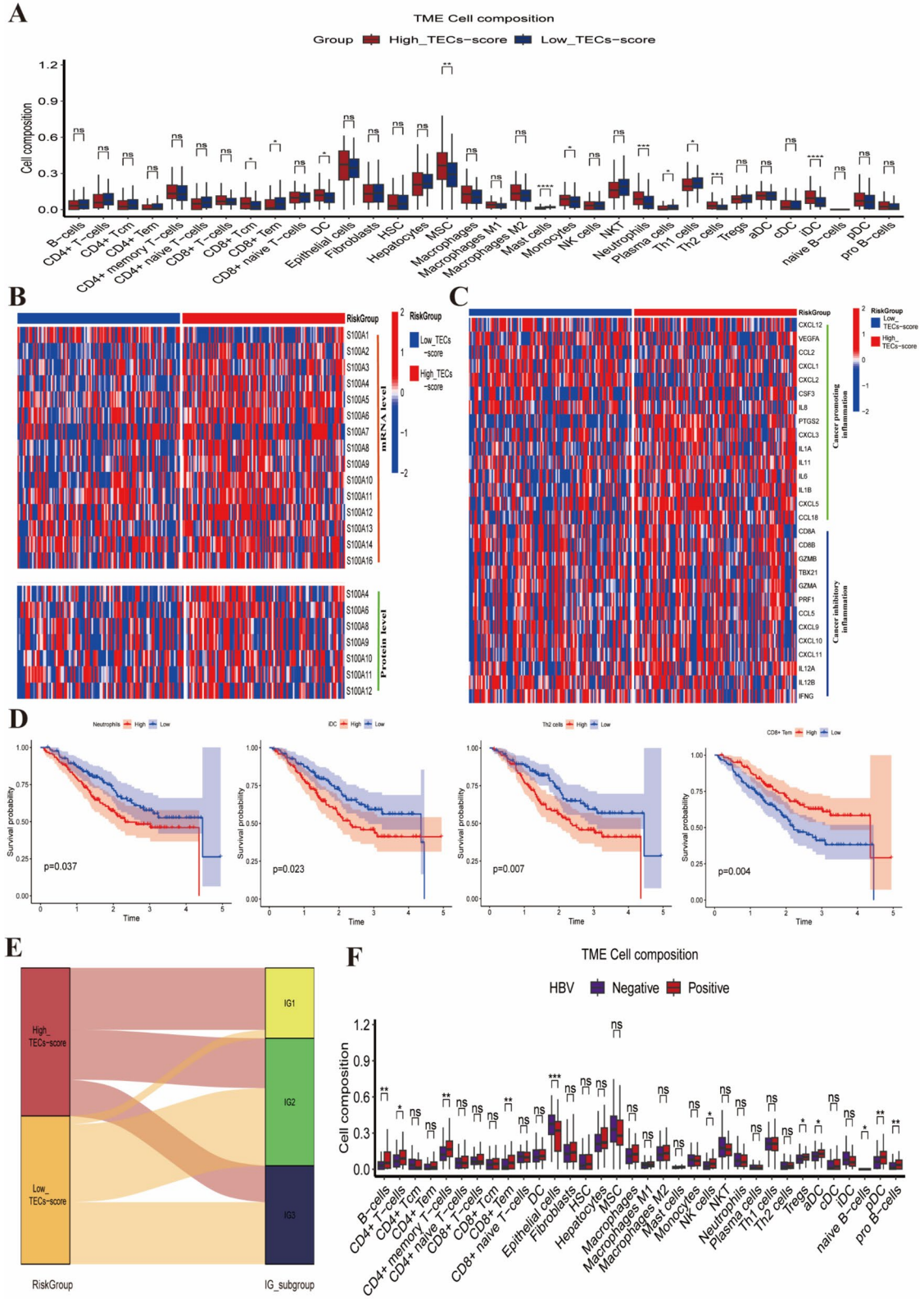

Fig. 4 (See legend on previous page.)

the infiltration of NK, CD4 + T, and CD8 + Tem cells (Fig. 5D). These findings suggest that CXCL12 overexpression might facilitate the infiltration of adaptive immune cells (e.g., NK, CD4 + T, and CD8 + Tem cells) while reducing neutrophils and iDCs.

Tumor immune dysfunction and exclusion (TIDE) is a predictor of the response to immune checkpoint inhibitors (ICIs) in various cancers. The low TEC score group had the lowest TIDE and dysfunction scores (Fig. 5E), indicating that patients with lower TEC scores might have less potential for immune escape and may respond more effectively to ICIs.

We further investigated genomic alterations that might be associated with immunological characteristics. The primary mutated genes in the low TEC score group were BAP1, TTN, and ARID1A, with an overall mutation frequency of 69.75% (Fig. 5F). In contrast, the primary mutated genes in the high TEC score group were KRAS, TP53, and TTN, with an overall mutation frequency of 84.87% (Fig. 5G). We hypothesized that KRAS mutations might be attributable to the poorer prognosis in ICC patients with high TEC scores. Kaplan–Meier curve analysis confirmed that patients with KRAS mutations had a worse prognosis (HR = 2.34, 95% CI 1.46–3.75, P = 0.00026, Fig. 5H), while patients with BAP1 mutations had a better prognosis (HR = 0.54, 95% CI 0.26–1.12, P = 0.093, Figure S4A). Immune infiltration analysis revealed that patients with KRAS mutations showed a significant reduction in NK, B, CD4 + T, and CD8 + Tem cells, along with a marked increase in neutrophil and iDC infiltration. Conversely, patients with BAP1 mutations exhibited a contrasting trend (Fig. 5I). ICC patients with KRAS mutations had higher TEC scores (Figure S4B), and poorer prognoses (HR = 3.19, 95% CI 1.36–7.46, P = 0.0048) (Fig. 5J). GSEA enrichment analysis revealed that ICC patients with KRAS mutations were predominantly enriched in pathways associated with myeloid cell-driven inflammatory responses, including neutrophil degranulation, inflammatory response, and TNF-α signaling via NF-κB signaling pathways. In contrast, BAP1 mutations in ICC patients were primarily enriched in the oxidative phosphorylation (OXPHOS) signaling pathway (Figure S4C), which is crucial for immune activation.

In summary, the TEC score can reflect the genomic mutation status in ICC patients. KRAS mutations may increase the infiltration of neutrophils and iDCs, while decreasing the infiltration of NK, CD4 + T, and CD8 + Tem cells. In contrast, BAP1 mutations and CXCL12 overexpression have contrasting effects.

TECs interact with various immune cells through the CXCL12/CXCR4 axis

To investigate the interactions between TECs and various immune cells within the TME, the CellChat package in R was used to perform a detailed analytical examination of cell–cell communication networks. The analysis found significant interactions between TECs and various immune cells in the TME (Fig. 6A). Further analysis of the receptor–ligand pairs involved in interactions between TECs and other cell types revealed that CXCL12/CXCR4 is the primary signaling axis through which TECs interact (Fig. 6B). TECs are the primary producers of CXCL12 (Figure S5A), and ICC patients with high CXCL12 expression levels have a better prognosis (Fig. 5B).

We extracted the feature matrix from scRNA-seq data and uploaded it to the CIBERSORTx online analysis platform (https://cibersortx.stanford.edu/) to evaluate the abundance of immune and stromal cells in each ICC sample. The correlation heatmap depicted a robust positive association between the prevalence of TECs and the concurrent abundance of T cells and myeloid cells, highlighting the interplay between these cells in the TME (Figure S5B). Spatial transcriptomic deconvolution analysis further confirmed the spatial co-localization of TECs with T cells and B cells (Figs. 6C–E, S5C). Additionally, TEC regions with high CXCL12 expression show a marked tendency for co-localization with T cells and B cells compared to regions with lower expression (Figure S5D). This suggests that TECs may interact with immune

(See figure on next page.)

Fig. 5 Analysis of the relationship between CXCL12 expression levels, KRAS mutations, and TME immune cell infiltration. **A** Violin plot comparing CXCL12 expression levels between high and low TEC score groups. **B** Kaplan–Meier curves illustrating the relationship between CXCL12 mRNA expression levels and patient prognosis. **C** Correlation bubble plot illustrating the relationship between CXCL12 and both oncogenes and tumor suppressor genes. **D** Correlation bubble plot showing the relationship between CXCL12 and various cell infiltrates. **E** Comparison of TIDE scores and Dysfunction scores in different TEC score groups. **F** Mutation waterfall plot showing the types and frequencies of gene mutations in the low TEC score group among 119 ICC patients. **G** Mutation waterfall plot showing the types and frequencies of gene mutations in the high TEC score group among 119 ICC patients. **H** Survival analysis under different gene mutation statuses, illustrated by Kaplan–Meier curves showing survival differences between patients with mutated and wild-type KRAS. **I** Comparison of immune cell infiltration in the TME among patients with wild-type genes, KRAS mutations, and BAP1 mutations. **J** Kaplan–Meier survival curve analysis comparing KRAS and BAP1 mutations with ICC patient prognosis

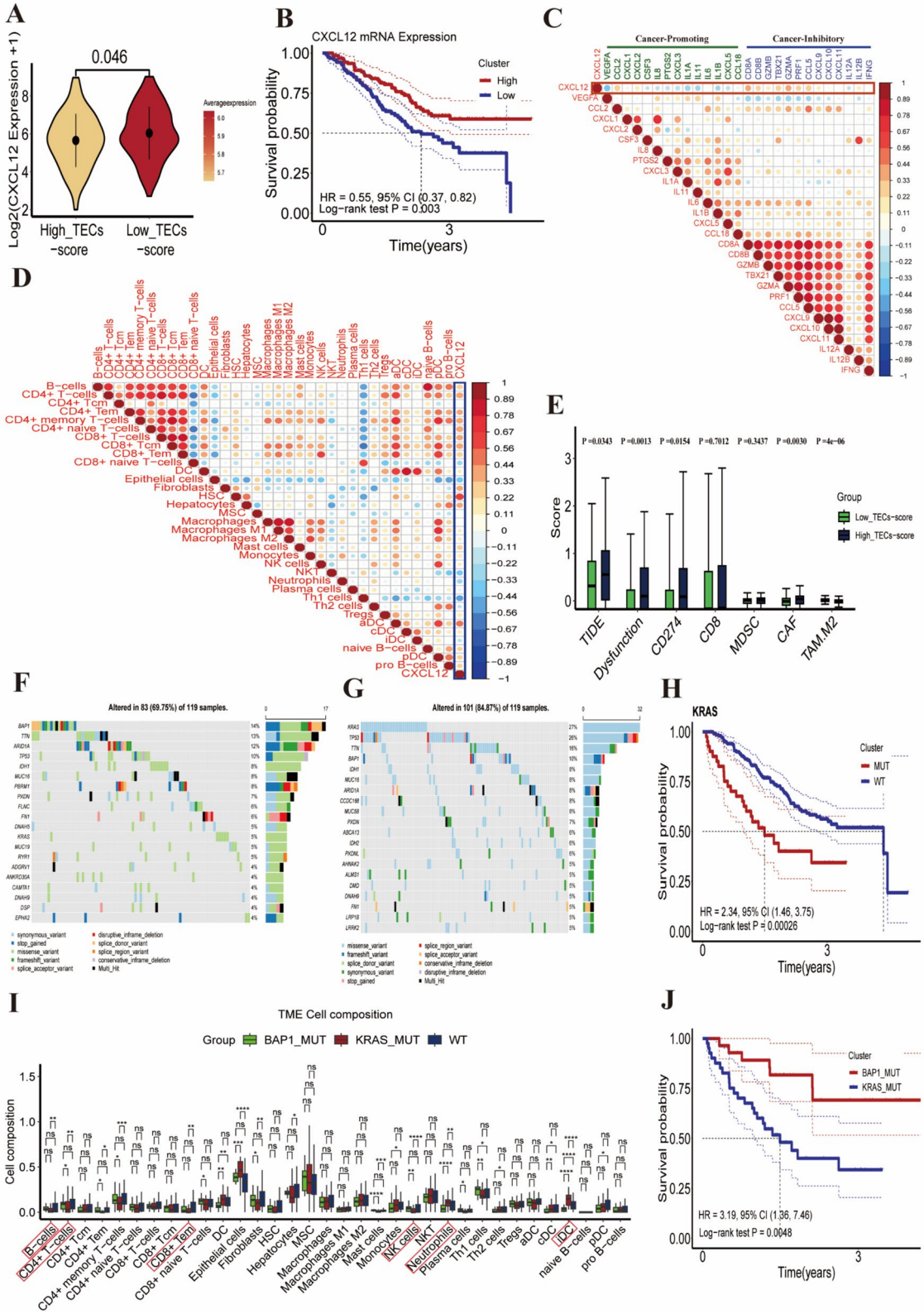

Fig. 5 (See legend on previous page.)

cells by secreting CXCL12, promoting immune activation and exhibiting an anti-tumor effect. Multiplex immunofluorescence staining experiments also confirmed the chemotactic effect of TECs with high CXCL12 expression levels on both T and B cells (Fig. 6F, Figure S5E–F), while those with low expression do not show this trend (Fig. 6G).

TEC.Sig predicts the response to immunotherapy

To investigate the association between the TEC.Sig and response to immunotherapy, we downloaded immunotherapy-related data from the GEO database for primary HCC (GSE202069), melanoma (MGSP: Melanoma Genome Sequencing Project), and bladder cancer (IMvigor210). The Cancerclass package in R software was used to calculate the z-score based on the expression levels of TEC.Sig genes for each tumor patient, to predict their responsiveness to immunotherapy. In the GSE202069 dataset, we found that the TEC.Sig could significantly predict immunotherapy outcomes in HCC patients, with an AUC of 0.96 (95% CI 0.91–1, Fig. 7A). Similarly, TEC.Sig also showed a high predictive value in the MGSP and IMvigor210 datasets, with AUC values of 0.78 (95% CI 0.74–0.82) and 0.73 (95% CI 0.7–0.76), respectively (Fig. 7B–C). Compared to previously reported gene sets used for predicting immunotherapy responses [38–41], TEC.Sig also exhibited larger AUC values (Figs. 7D–F, S6A–C). These results indicate that TEC.Sig demonstrates a reliable level of accuracy for predicting the immunotherapy response.

Discussion

While exploring ICC pathogenesis and treatment strategies, our study highlights the critical role of the TME, particularly the heterogeneity and functional diversity of TECs. ICC, a malignant tumor derived from secondary bile duct epithelial cells, is predominantly an adenocarcinoma that can be classified into large duct and small duct types [19, 20, 42]. ICC accounts for approximately 10–15% of primary liver cancers and 20% of cholangiocarcinomas [43, 44]. Despite surgical resection being the only potentially curative treatment for ICC, the high recurrence rate (over 60%) severely impacts long-term patient survival, with a five-year survival rate of only about 30% [45, 46]. This therapeutic limitation underscores the need for a deeper understanding of the ICC TME, in order to develop more effective treatment strategies.

Our study used single-cell sequencing technology to reveal the functional heterogeneity of TECs within the ICC TME, providing a novel perspective for elucidating their involvement in angiogenesis, immune cell interactions, tumor cell invasion and metastatic behavior, and treatment resistance development [47–49]. In recent years, the role of the TME in ICC growth and progression, particularly the genetic stability of TME components (such as endothelial cells), has attracted increased attention, which makes them potential therapeutic targets [50]. Biologic therapies such as bevacizumab that target angiogenesis have shown positive effects in clinical trials and preclinical models of various cancers. Changes in the TEC phenotype and functional characteristics reflect alterations at the transcriptional level, highlighting their complex role in tumor development [51].

The TEC score, an innovative prognostic biomarker based on TEC gene expression patterns, can predict ICC patient prognosis and provide essential evidence for clinical decision-making and risk stratification. The TEC score is expected to become an effective tool for guiding ICC treatment regimen selection and prognostic assessment in the future. Additionally, the potential of the TEC.Sig to predict the response to immunotherapy in ICC patients offers new insights for optimizing immunotherapy regimens and reducing unnecessary side effects. Future research should further validate the predictive efficacy of TEC.Sig in larger sample populations and explore its application in other cancer types.

Our study found a significant association between KRAS and BAP1 mutations and the ICC immune microenvironment. KRAS mutations may be associated with a pro-inflammatory and immunosuppressive state of TECs, whereas BAP1 mutations may be linked to immune activation and anti-tumor responses. KRAS mutations are associated with the recruitment of myeloid cells and MDSCs to the TME, driving immunosuppression [52]. TP53 and KRAS co-mutations might promote

(See figure on next page.)

Fig. 6 TECs interact with T cells and B cells. **A** Interaction network diagram depicting the relationships between TECs and other cell types. **B** Dot plot illustrating the strength of interactions, with a focus on the CXCL12/CXCR4 signaling axis. **C** Histological image of ICC tumor samples. **D** Spatial transcriptomic analysis showing the spatial distribution of endothelial cell signatures, B cell signatures, and T cell signatures within the ICC tissue. **E** Spatial maps showcasing the signature expression of VWF and CLDN5 (endothelial markers), CD79A (B cell marker), and CD8A (T cell marker), illustrate the spatial co-localization of these cells within the tissue. **F** Immunofluorescence staining experiments demonstrated that endothelial cells in tumor tissues secrete higher levels of CXCL12, which is associated with increased infiltration of T cells and B cells around the endothelial cells. **G** Immunofluorescence staining experiments showed that endothelial cells in tumor tissues secrete lower levels of CXCL12, accompanied by reduced infiltration of T cells and B cells around the endothelial cells

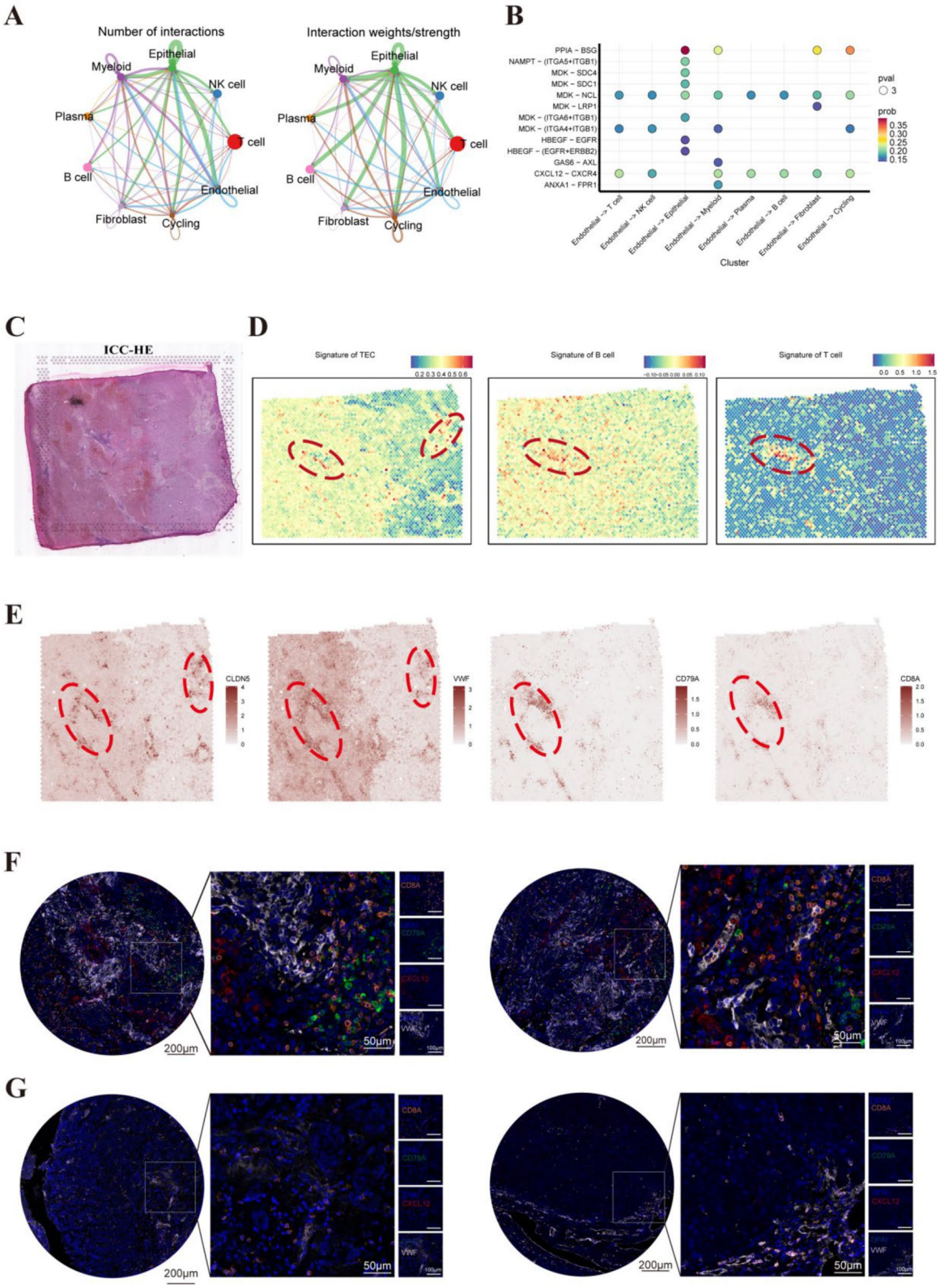

Fig. 6 (See legend on previous page.)

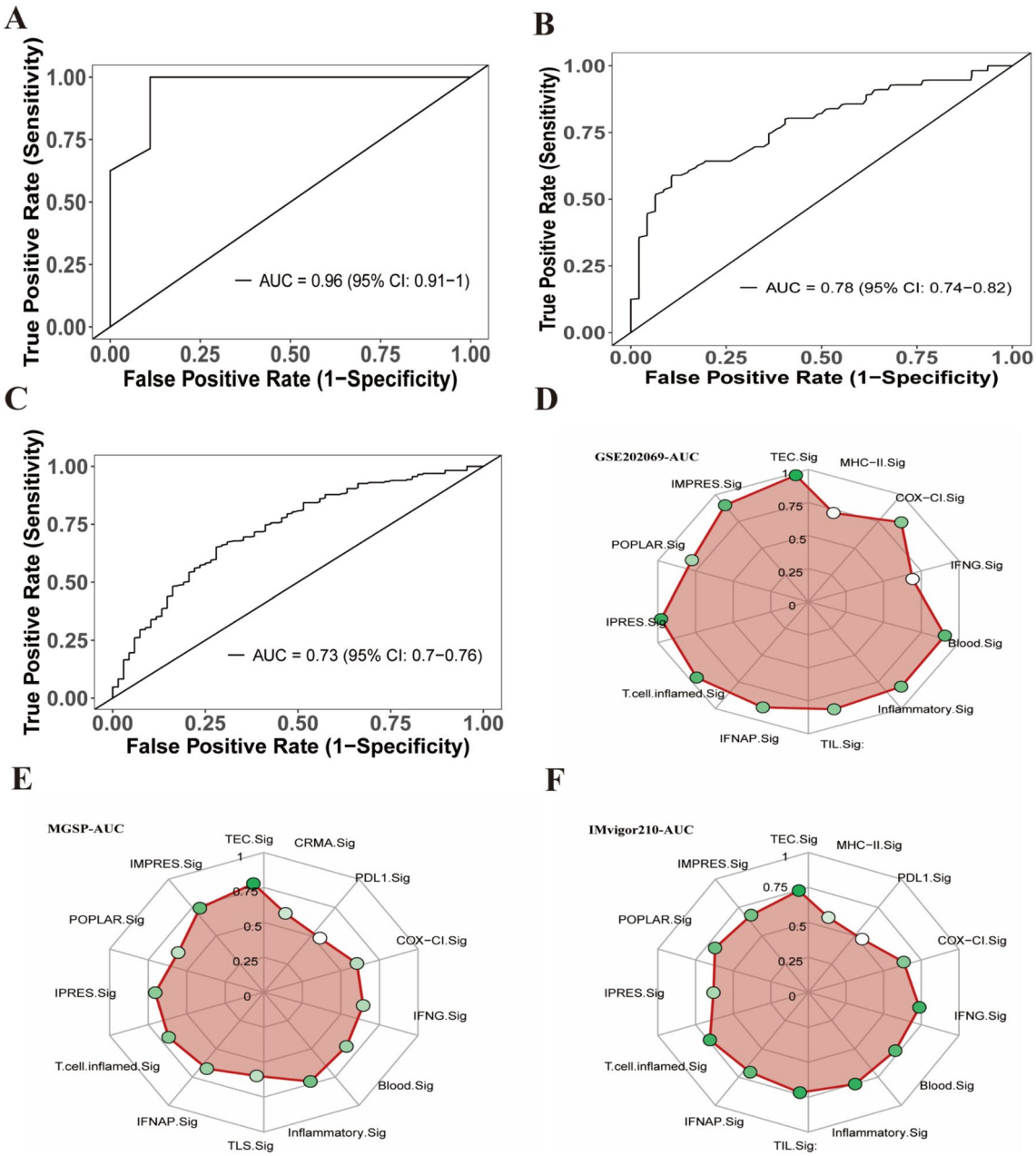

Fig. 7 Performance evaluation of the prediction model. **A** ROC curve of the prediction model using the GSE202069 dataset, with an AUC value of 0.96. **B** ROC curve of the prediction model using the MGSP dataset, with an AUC value of 0.78. **C** ROC curve of the prediction model using the IMvigor210 dataset, with an AUC value of 0.73. **D** Comparison of AUC values of the prediction model on the GSE202069 dataset using radar charts, demonstrating the performance of the TEC.Sig compared to other models used for predicting the immunotherapeutic response. **E** Comparison of AUC values of the prediction model on the MGSP dataset using radar charts, demonstrating the performance of the TEC. Sig compared to other models used for predicting the immunotherapy response. **F** Comparison of AUC values of the prediction model on the IMvigor210 dataset using radar charts, demonstrating the performance of the TEC.Sig compared to other models used for predicting the immunotherapy response

extrahepatic metastasis of ICC through the activation of the integrin-FAK-SRC signaling pathway [17, 53]. BAP1, a tumor suppressor gene, expresses a deubiquitinating enzyme and is mutated or deleted in various tumors, and is directly related to tumorigenesis [54, 55]. We observed that patients with BAP1 mutations had a better prognosis, which may be related to reduced monocytic cells and decreased chronic inflammation in tumors. Meanwhile,

BAP1 mutations may lead to tumor cells producing more immunogenic neoantigens, thereby initiating a stronger anti-tumor immune response [56, 57].

Through methods such as single-cell sequencing, spatial transcriptomic sequencing, and multiplex immunofluorescence staining, we confirmed that in the ICC TME, TECs with high CXCL12 expression exhibit chemotactic effects on T cells and B cells. These TECs interact with immune cells by secreting CXCL12, promoting immune cell activation and exhibiting a significant anti-tumor immune effect. However, it should be noted that the CXCL12/CXCR4 axis exhibits heterogeneity across different cancer microenvironments and might play a pro-tumor role in certain tumors [58]. For example, in prostate cancer, the CXCL12/CXCR4 signaling axis has been found to play a role in promoting tumor angiogenesis [58–60]. In gastrointestinal malignancies, CXCL12 binds to the CXCR4 receptor on the tumor cell surface, activating anti-apoptotic signaling pathways, while promoting epithelial-mesenchymal transitions, ultimately leading to the resistance of tumor cells to the immune system [61].

In conclusion, our study reveals the complex role of TECs in the ICC TME and provides new biomarkers and potential targets for ICC treatment. Several potential limitations were identified, including the limited sample size for both scRNA-seq and spatial transcriptomic sequencing. Additionally, this study did not address the specific molecular mechanisms by which the downstream signaling pathways of the CXCL12/CXCR4 axis activate immune cells. Future studies can explore the interactions between TECs and immune cells and assess the use of TECs as biomarkers and targets for ICC treatment.

Supplementary Information

The online version contains supplementary material available at https://doi.org/10.1186/s12967-024-05750-2.

Additional file 1: Figure S1. Distribution of different cell types in ICC.Quality control metrics for scRNA-seq data across different cell types identified in the ICC TME.t-SNE plot for classifying cell types based on the expression levels of typical marker genes.Boxplot of ROGUE scores representing the purity of different endothelial cell subpopulations.Dot plot showing the expression of three key genesacross different cell types.The violin plot illustrates a comparison of the combined expression levels of CXCL12, TCF7L2, and SYNPO across different cell types. Figure S2. Relationship between the TEC score, survival time, and clinical characteristics.Diagram depicting the relationships between risk factors in the training set, including ranked plot showing the high and low distribution of TEC scores, scatter plots of the distribution of patient survival, and heatmaps showing changes in gene expression levels with TEC scores.Time-dependent ROC curve of TEC scores, with an AUC value of 0.75and 0.79.A comparison of survival curves between high and low TEC score groups in the GSE89749 dataset, demonstrated using Kaplan-Meier curves showing a poorer prognosis for the high TEC score group.Time-dependent ROC curve of TEC scores in the GSE89749 dataset, with an AUC value of 0.57and 0.65. Correlation between TEC scores and CEA levels, demonstrated using a scatter plot showing the positive correlation between the two.Correlation between TEC scores and CA19-9 levels, demonstrated using a scatter plot showing the positive correlation between the two.Forest plot of the HR and p-value between different clinical characteristic groups, with Cox univariate regression analysis demonstrating how significant clinical factors affect ICC patient prognosis.Cox multivariate regression analysis further confirmed the independent risk factors affecting ICC patient prognosis. Figure S3. GSEA of the high TEC score group.Enrichment plot demonstrating significant enrichment of the high TEC score group in the inflammatory response pathway.Enrichment plot highlighting significant enrichment of the high TEC score group in the IL6/JAK/STAT3 signaling pathway.Enrichment plot demonstrating significant enrichment of the high TEC score group in the TGF-β signaling pathway.Enrichment plot revealing significant enrichment of the high TEC score group in the TNFα/NF-κB signaling pathway.It illustrates the relationship between neutrophil infiltration and iDC infiltration with the expression levels of immunosuppressive genes in the TME of ICC.Correlation heatmap showing the relationships between CXCL12 expression, TEC score, and the expression of the three genes constituting TEC.Sig. Figure S4. Impact of different gene mutation statuses on the TEC score and patient prognosis.Impact of BAP1 mutations on the survival time, demonstrated using Kaplan-Meier curves showing the differences in survival between patients with BAP1 mutations and wild-type genes.Comparison of TEC scores between patients with BAP1 and KRAS mutations, presented as a bar graph showing significantly higher TEC scores in patients with KRAS mutations, compared to those with BAP1 mutations.GSEA enrichment analysis demonstrating differential pathway enrichment in patients with KRAS and BAP1 mutations. Figure S5. CXCL12 expression and spatial distribution in TECs.Violin plot demonstrating high CXCL12 expression in endothelial cells compared to other cell types.Correlation heatmap illustrating the associations between TEC abundance and other cell types in the TME.Spatial transcriptomics map revealing the distribution of different cell types in tissue sections, with all cells segregating into five clusters.Spatial expression map of CXCL12 within the TME.In the multiplex immunofluorescence staining experiment, the analysis showed a positive correlation trend between CXCL12 and CD8 expression.In the multiplex immunofluorescence staining experiment, a significant positive correlation was observed between CXCL12 and CD79A expression. Figure S6. ROC curves of TEC.Sig for predicting immunotherapy responses in different datasets.ROC curve of TEC.Sig in the GSE202069 dataset, with an AUC value of 0.96.ROC curve of TEC.Sig in the MGSP dataset, with an AUC value of 0.78.ROC curve of TEC.Sig in the IMvigor210 dataset, with an AUC value of 0.73

Acknowledgements
We would like to express our deepest gratitude to everyone who supported us throughout this study. Special thanks to the following individuals for their invaluable contributions: Biao Gao, Zihe Meng, Yafei Wang, Tiaoyu Jiao, Junfeng Li, Xuerui Li, Yinbiao Cao, Xianzhou Zhang, Chonghui Li, and Shichun Lu for their collaborative efforts and dedication to this research project. To our institutions and colleagues who provided us with the necessary resources and support.

Author contributions
Hao Jiang, Biao Gao, Zihe Meng, and Yafei Wang contributed to the conception and design; Hao Jiang, Biao Gao, Yafei Wang, and Tianyu Jiao contributed to data analysis and interpretation. Zihe Meng, Xuerui Li, Yinbiao Cao, Junfeng Li, and Hao Jiang contributed to the provision of study materials and execution of experiments. Hao Jiang, Xianzhou Zhang, Chonghui Li, and Shichun Lu drafted and revised the manuscript. All authors read and approved the final manuscript.

Funding
No funding.

Data availability
The datasets used during the current study are available from the corresponding author on reasonable request.

Declarations

Ethics approval and consent to participate

This study was conducted in accordance with the principles of the Declaration of Helsinki. Ethical approval for this study was obtained from the Ethics Committee of Medical School of Chinese People's Liberation Army (PLA), approval number (S2018-111-01). All participants provided written informed consent before enrollment in the study.

Competing interests

The authors have no conflicts to report.

Received: 11 July 2024 Accepted: 8 October 2024
Published online: 19 October 2024

References

1. Razumilava N, Gores GJ. Cholangiocarcinoma. Lancet. 2014;383(9935):2168–79.
2. Siegel RL, Miller KD, Fuchs HE, et al. Cancer statistics, 2021. CA Cancer J Clin. 2021;71(1):7–33.
3. Jing CY, Fu YP, Huang JL, et al. Prognostic nomogram based on histological characteristics of fibrotic tumor stroma in patients who underwent curative resection for intrahepatic cholangiocarcinoma. Oncologist. 2018;23(12):1482–93.
4. de Jong MC, Nathan H, Sotiropoulos GC, et al. Intrahepatic cholangiocarcinoma: an international multi-institutional analysis of prognostic factors and lymph node assessment. J Clin Oncol. 2011;29(23):3140–5.
5. Witjes CD, Karim-Kos HE, Visser O, et al. Intrahepatic cholangiocarcinoma in a low endemic area: rising incidence and improved survival. HPB. 2012;14(11):777–81.
6. Kurebayashi Y, Ojima H, Tsujikawa H, et al. Landscape of immune microenvironment in hepatocellular carcinoma and its additional impact on histological and molecular classification. Hepatology. 2018;68(3):1025–41.
7. Høgdall D, Lewinska M, Andersen JB. Desmoplastic tumor microenvironment and immunotherapy in cholangiocarcinoma. Trends Cancer. 2018;4(3):239–55.
8. Sirica AE, Gores GJ. Desmoplastic stroma and cholangiocarcinoma: clinical implications and therapeutic targeting. Hepatology. 2014;59(6):2397–402.
9. Morse MA, Sun W, Kim R, et al. The role of angiogenesis in hepatocellular carcinoma. Clin Cancer Res. 2019;25(3):912–20.
10. Gracia-Sancho J, Caparrós E, Fernández-Iglesias A, et al. Role of liver sinusoidal endothelial cells in liver diseases. Nat Rev Gastroenterol Hepatol. 2021;18(6):411–31.
11. Huang SL, Wang YM, Wang QY, et al. Mechanisms and clinical trials of hepatocellular carcinoma immunotherapy. Front Genet. 2021;12:691391.
12. Heidegger I, Pircher A, Pichler R. Targeting the tumor microenvironment in renal cell cancer biology and therapy. Front Oncol. 2019;9:490.
13. Pircher A, Hilbe W, Heidegger I, et al. Biomarkers in tumor angiogenesis and anti-angiogenic therapy. Int J Mol Sci. 2011;12(10):7077–99.
14. Finn RS, Qin S, Ikeda M, et al. Atezolizumab plus bevacizumab in unresectable hepatocellular carcinoma. N Engl J Med. 2020;382(20):1894–905.
15. Cheng AL, Qin S, Ikeda M, et al. Updated efficacy and safety data from IMbrave150: atezolizumab plus bevacizumab vs. sorafenib for unresectable hepatocellular carcinoma. J Hepatol. 2022;76(4):862–73.
16. Lin J, Dai Y, Sang C, et al. Multimodule characterization of immune subgroups in intrahepatic cholangiocarcinoma reveals distinct therapeutic vulnerabilities. J Immunother Cancer. 2022;10(7): e004892.
17. Dong L, Lu D, Chen R, et al. Proteogenomic characterization identifies clinically relevant subgroups of intrahepatic cholangiocarcinoma. Cancer Cell. 2022;40(1):70-87.e15.
18. Mariathasan S, Turley SJ, Nickles D, et al. TGFβ attenuates tumour response to PD-L1 blockade by contributing to exclusion of T cells. Nature. 2018;554(7693):544–8.
19. Moris D, Palta M, Kim C, et al. Advances in the treatment of intrahepatic cholangiocarcinoma: an overview of the current and future therapeutic landscape for clinicians. CA Cancer J Clin. 2023;73(2):198–222.
20. Brindley PJ, Bachini M, Ilyas SI, et al. Cholangiocarcinoma. Nat Rev Dis Prim. 2021;7(1):65.
21. Macias RIR, Cardinale V, Kendall TJ, et al. Clinical relevance of biomarkers in cholangiocarcinoma: critical revision and future directions. Gut. 2022;71(8):1669–83.
22. Wang Y, Yu H, Xie X, et al. Plasmalemma vesicle-associated protein promotes angiogenesis in cholangiocarcinoma via the DKK1/CKAP4/PI3K signaling pathway. Oncogene. 2021;40(25):4324–37.
23. Zhang M, Yang H, Wan L, et al. Single-cell transcriptomic architecture and intercellular crosstalk of human intrahepatic cholangiocarcinoma. J Hepatol. 2020;73(5):1118–30.
24. Zeng Q, Mousa M, Nadukkandy AS, et al. Understanding tumour endothelial cell heterogeneity and function from single-cell omics. Nat Rev Cancer. 2023;23(8):544–64.
25. Schaaf MB, Houbaert D, Meçe O, et al. Autophagy in endothelial cells and tumor angiogenesis. Cell Death Differ. 2019;26(4):665–79.
26. Wang X, Chen Z, Xu J, et al. SLC1A1-mediated cellular and mitochondrial influx of R-2-hydroxyglutarate in vascular endothelial cells promotes tumor angiogenesis in IDH1-mutant solid tumors. Cell Res. 2022;32(7):638–58.
27. Orso F, Quirico L, Dettori D, et al. Role of miRNAs in tumor and endothelial cell interactions during tumor progression. Semin Cancer Biol. 2020;60:214–24.
28. Cleveland AH, Fan Y. Reprogramming endothelial cells to empower cancer immunotherapy. Trends Mol Med. 2024;30(2):126–35.
29. Cabrerizo-Granados D, Peña R, Palacios L, et al. Snail1 expression in endothelial cells controls growth, angiogenesis and differentiation of breast tumors. Theranostics. 2021;11(16):7671–84.
30. Zhu Y, Yang J, Xu D, et al. Disruption of tumour-associated macrophage trafficking by the osteopontin-induced colony-stimulating factor-1 signalling sensitises hepatocellular carcinoma to anti-PD-L1 blockade. Gut. 2019;68(9):1653–66.
31. Zhong C, Niu Y, Liu W, et al. S100A9 derived from chemoembolization-induced hypoxia governs mitochondrial function in hepatocellular carcinoma progression. Adv Sci. 2022;9(30): e2202206.
32. Denk D, Greten FR. Inflammation: the incubator of the tumor microenvironment. Trends Cancer. 2022;8(11):901–14.
33. Ritter B, Greten FR. Modulating inflammation for cancer therapy. J Exp Med. 2019;216(6):1234–43.
34. Manjili SH, Isbell M, Ghochaghi N, et al. Multifaceted functions of chronic inflammation in regulating tumor dormancy and relapse. Semin Cancer Biol. 2022;78:17–22.
35. Kiely M, Lord B, Ambs S. Immune response and inflammation in cancer health disparities. Trends Cancer. 2022;8(4):316–27.
36. Zhang Q, He Y, Luo N, et al. Landscape and dynamics of single immune cells in hepatocellular carcinoma. Cell. 2019;179(4):829-45.e20.
37. Koenen RR, Weber C. Therapeutic targeting of chemokine interactions in atherosclerosis. Nat Rev Drug Discov. 2010;9(2):141–53.
38. Bonavita E, Bromley CP, Jonsson G, et al. Antagonistic inflammatory phenotypes dictate tumor fate and response to immune checkpoint blockade. Immunity. 2020;53(6):1215-29.e8.
39. Auslander N, Zhang G, Lee JS, et al. Robust prediction of response to immune checkpoint blockade therapy in metastatic melanoma. Nat Med. 2018;24(10):1545–9.
40. Hugo W, Zaretsky JM, Sun L, et al. Genomic and transcriptomic features of response to anti-PD-1 therapy in metastatic melanoma. Cell. 2017;168(3):542.
41. Johnson DB, Estrada MV, Salgado R, et al. Melanoma-specific MHC-II expression represents a tumour-autonomous phenotype and predicts response to anti-PD-1/PD-L1 therapy. Nat Commun. 2016;7:10582.
42. Vithayathil M, Khan SA. Current epidemiology of cholangiocarcinoma in Western countries. J Hepatol. 2022;77(6):1690–8.
43. Siegel RL, Miller KD, Fuchs HE, et al. Cancer statistics, 2022. CA Cancer J Clin. 2022;72(1):7–33.
44. Amin MB, Greene FL, Edge SB, et al. The eighth edition AJCC cancer staging manual: continuing to build a bridge from a population-based to a more "personalized" approach to cancer staging. CA Cancer J Clin. 2017;67(2):93–9.
45. Florio AA, Ferlay J, Znaor A, et al. Global trends in intrahepatic and extrahepatic cholangiocarcinoma incidence from 1993 to 2012. Cancer. 2020;126(11):2666–78.

46. Chun YS, Javle M. Systemic and adjuvant therapies for intrahepatic cholangiocarcinoma. Cancer Control. 2017;24(3):1073274817729241.
47. Saxton RA, Sabatini DM. mTOR signaling in growth, metabolism, and disease. Cell. 2017;169(2):361–71.
48. Naik S, Larsen SB, Gomez NC, et al. Inflammatory memory sensitizes skin epithelial stem cells to tissue damage. Nature. 2017;550(7677):475–80.
49. Routy B, le Chatelier E, Derosa L, et al. Gut microbiome influences efficacy of PD-1-based immunotherapy against epithelial tumors. Science. 2018;359(6371):91–7.
50. de Gregorio V, Urciuolo F, Netti PA, et al. In vitro organotypic systems to model tumor microenvironment in human papillomavirus (HPV)-related cancers. Cancers. 2020;12(5):1150.
51. Hida K, Kikuchi H, Maishi N, et al. ATP-binding cassette transporters in tumor endothelial cells and resistance to metronomic chemotherapy. Cancer Lett. 2017;400:305–10.
52. Pylayeva-Gupta Y, Lee KE, Hajdu CH, et al. Oncogenic Kras-induced GM-CSF production promotes the development of pancreatic neoplasia. Cancer Cell. 2012;21(6):836–47.
53. Tanaka M, Kunita A, Yamagishi M, et al. KRAS mutation in intrahepatic cholangiocarcinoma: linkage with metastasis-free survival and reduced E-cadherin expression. Liver Int. 2022;42(10):2329–40.
54. Carbone M, Yang H, Pass HI, et al. BAP1 and cancer. Nat Rev Cancer. 2013;13(3):153–9.
55. Sahtoe DD, van Dijk WJ, Ekkebus R, et al. BAP1/ASXL1 recruitment and activation for H2A deubiquitination. Nat Commun. 2016;7:10292.
56. Hsiue EH, Wright KM, Douglass J, et al. Targeting a neoantigen derived from a common TP53 mutation. Science. 2021;371(6533):eabc8697.
57. Schumacher TN, Schreiber RD. Neoantigens in cancer immunotherapy. Science. 2015;348(6230):69–74.
58. Heidegger I, Fotakis G, Offermann A, et al. Comprehensive characterization of the prostate tumor microenvironment identifies CXCR4/CXCL12 crosstalk as a novel antiangiogenic therapeutic target in prostate cancer. Mol Cancer. 2022;21(1):132.
59. Yang Y, Li J, Lei W, et al. CXCL12-CXCR4/CXCR7 axis in cancer: from mechanisms to clinical applications. Int J Biol Sci. 2023;19(11):3341–59.
60. Uygur B, Wu WS. SLUG promotes prostate cancer cell migration and invasion via CXCR4/CXCL12 axis. Mol Cancer. 2011;10:139.
61. Daniel SK, Seo YD, Pillarisetty VG. The CXCL12-CXCR4/CXCR7 axis as a mechanism of immune resistance in gastrointestinal malignancies. Semin Cancer Biol. 2020;65:176–88.

Publisher's Note